

Article

A Sparse Autoencoder and Softmax Regression based Diagnosis Method for the Attachment on the Blades of Marine Current Turbine

Yilai Zheng¹, Tianzhen Wang^{1,*}, Bin Xin¹, Tao Xie¹, Yide Wang²

¹ Department of Electrical Automation, Shanghai Maritime University; tzwang@shmtu.edu.cn

² Institut d'Electronique et Telecommunications de Rennes (IETR), University of Nantes; yide.wang@polytech.univ-nantes.fr

* Correspondence: wtz0@sina.com; Tel.: +862138282640

Abstract: The development and application of marine current energy are attracting more and more attention in the world. Due to the hardness of its working environment, it is important and difficult to study the fault diagnosis of marine current generation system. In this paper, underwater image is chosen as the fault diagnosing signal after different sensors are compared. This paper proposes a diagnosis method based on the sparse autoencoder (SA) and softmax regression (SR). The SA is used to extract the features and SR is used to classify them. Images are used to monitor whether the blade is attached by benthos and to determine its corresponding degree of attachment. Compared with the other techniques, experiment results show that the proposed method can diagnose the blade attachment with higher accuracy.

Keywords: marine current turbine; blade attachment; sparse autoencoder; softmax regression

1. Introduction

Nowadays, reducing carbon emission becomes a consensus in the world. It is urgent to adjust the energy structure, reduce the dependence on fossil energy and increase the use of sustainable energy, which makes the wind, solar, marine current energies [1]-[3] more and more attractive. The system of wind and solar energies is greatly affected by the environment, occupies a lot of land resources, and brings noise and visual pollution to the surrounding residents. The marine current energy can avoid these problems. The marine current mainly refers to the steady flow in the submarine channel and the regular flow of water caused by tides [4]. The flow of the marine current is stable, and the flow rate is kept within a certain range all year round [5], therefore the power can be continuously generated [6], [7]. Marine current energy is an inexhaustible green energy resource and marine current turbine (MCT) is mainly independent of weather conditions [8]. However, compared with the terrestrial environment, the undersea working environment is more complex. In addition to the traditional generator faults, MCT system is also influenced by the marine environment, such as attachment, biofouling [9], [10], etc., affecting the normal operation of electrical equipment. On the other hand, the marine current generation system is affected by the sun, lunar gravity and surge, resulting in the instability of the current flow rate [11], [12], which makes the MCT work in complicated environment during a long time, which means that the detection and diagnosis of faults of MCT are more difficult. Once a fault occurs, it can cause great damage to the whole system if it is not found and dealt with in time. The conventional faults caused by attachment include rotor asymmetries, increased surface roughness and deformation of blade [13]. In addition, the metal parts are much easier corroded by attachment [8]. When the blades are attached by sea creatures which gradually form the biofouling, the blade imbalance and hydrodynamic effect will result in the output

power imbalance. When the blade is affected by attachment, the amplitude and frequency of the output voltage are reduced. The attachment will reduce the efficiency of the absorption of kinetic energy from flow and reduce rotational speed of the blade. At same time, a small change of the flow rate will have a great influence on the output voltage [14]. If the blade attachment is not found in time and cleaned up quickly, the situation of biological deposition becomes serious and its output voltage waveform will be distorted.

At present, there are few researches on the fault diagnosis of MCT. Reference [15] proposes a fault detection method, based on empirical mode decomposition (EMD) and spectral analysis, for MCT under the condition of wave and turbulence. A mode-correlation principal component analysis method is proposed to monitor MCT under random occurrence of turbulence and wave [16]. Reference [17] uses time domain, time-frequency domain and angle domain features to detect faults which achieves good performance for MCT under complex condition. But those methods only detect the imbalance fault. Particularly in reference [17], only two categories of faults (imbalance fault 1% and 3%) are considered, which means that even-distributed attachment cannot be detected. Meanwhile, those methods still need human to analyze the observed results. Reference [42] proposed a modified extended kalman filter (MEKF) fault detection strategy, but this method needs extra electric circuit, which is a challenge in undersea environment.

On the other hand, the electrical and mechanical signals are not always enough to diagnose faults in environment with strong currents and complex spatiotemporal variability [18,19]. The undersea radio signals cannot travel far due to the absorption losses [20] and many acoustic signals are lost due to partial band interference [20]. Therefore, this paper proposes to use image as the fault diagnosing signal, because underwater camera has been widely used which provides an effective nondestructive means for underwater measurement in various scenarios [21]. In reference [22], a lithium polymer battery of 10000 mAh capacity is used for camera battery and the camera can work for up to 10 days if it is controlled to record 60 seconds video every two hours under the sea with depth between 1000m and 1800m. Traditional image classification methods include BP neural network [23], support vector machine (SVM) [24], principal component analysis [25], etc. BP neural network and SVM require a great number of parameters when the dimension of input is large. Convolutional neural network (CNN), a more recent classification method, achieves high accuracy in image classification by stacking convolutional layers or blocks [26], [27], which also means a big number of parameters and very high computational complexity [28]. In this paper, a diagnosis method based on a sparse autoencoder (SA) and softmax regression (SR) is proposed to diagnose whether the blade of the MCT is attached by benthos and to determine its corresponding degree of attachment. The SA is adopted to extract the features which will be classified by SR. Theoretical analysis and experimental results show the effectiveness of the proposed method.

This paper is an extended version of reference [29] and the rest of paper is organized as follows. Section II introduces the problems of blade attachment. Section III describes the proposed method. Section IV presents the platform and gives some experimental results and comparison. The conclusions are drawn in the final section.

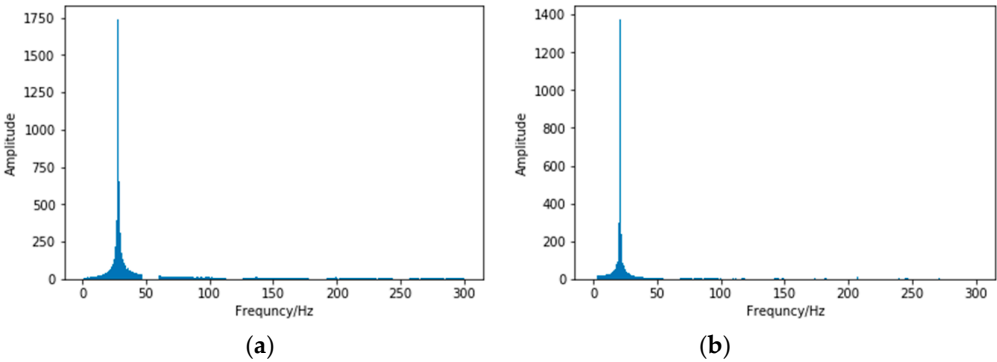
2. Problem description on Blade attachment of MCT

At present, MCT fault detection mainly focuses on imbalance faults, which is based on electrical signal. But electrical signal is affected by the complex environment, which results in difficulties to diagnose the attachment with similar degrees. In [17], two attachment degrees are set, which can be explicitly distinguished under waves, but cannot be distinguished under condition of turbulence.

The increased surface roughness and deformation of blade are also important in addition to the rotor asymmetries caused by imbalance attachment. These two kinds of faults are mainly caused by symmetrical or uniform attachment. For example, the output voltage signals are sampled under health condition and uniform attachment; FFT is used to analyze the sampled signal, the results are shown in Figure 1.

Although the amplitude and main frequency of the output voltage for uniform attachment are lower, the frequency behavior is better in terms of harmonic components distribution and amplitude.

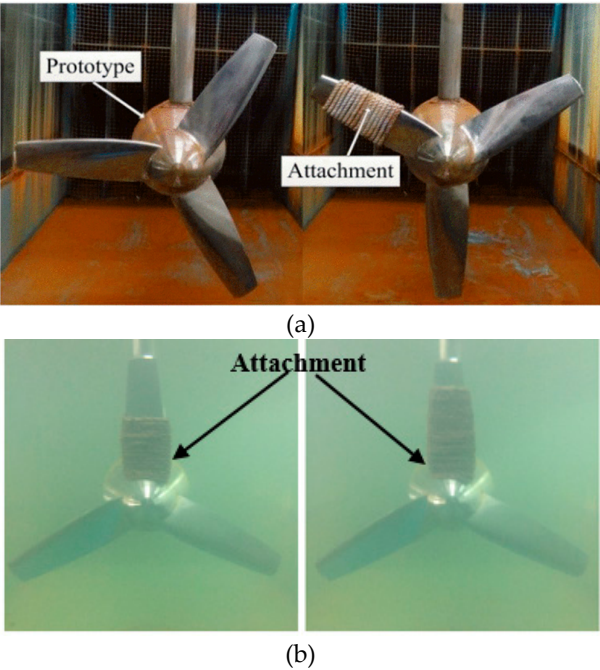
95 That leads to the challenge of accurate diagnosis based on electrical signal under increased surface
96 roughness and deformation of blade. Acoustic signal is also used to diagnose faults under increased
97 surface roughness of blade for wind turbine [13], however, many acoustic signals are lost in the
98 undersea environment [20].
99



100
101
102 **Figure 1.** The output voltage of MCT under different condition: (a) The output voltage under health
103 condition; (b) The output voltage with uniform attachment.

104 Image as fault diagnosing signal is proposed in this paper. The undersea environment is
105 different from that on land, there is no source of light. Underwater imaging systems have to rely on
106 the artificial light to provide illumination, which brings problems due to light absorption, light
107 reflection, bending, light scattering and poor visibility [30]. Therefore, image feature extraction
108 method is a key point for diagnosing faults based on image classification.

109 In real situation, the thickness is not considered as a parameter. Fig. 3 shows real situation, when
110 marine current turbine is salvaged from undersea. MCT is only with thin brown attachment. In
111 addition, blades fouled with a 1.1 mm thick layer of lithium grease impregnated with diatomaceous
112 earth as an approximation of slime growth in Fig. 4. The Fig. 4 shows that attachment grows from the
113 center and outwards. Because of above reasons and real biofilms were not able to be grown on a
114 rotating turbine or be tested in the towing tank [42], brown rope is used to simulate attachment.



115
116
117
118
119 **Figure 2.** Image under different environment: (a) Waterborne image [17]; (b) Underwater image.

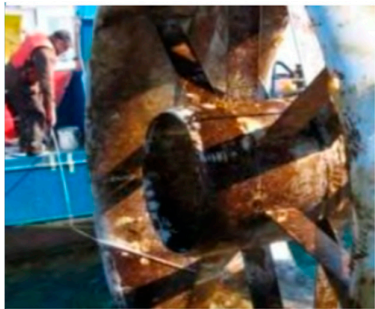


Fig. 3 Biofouling & Erosion for MCECS [8]

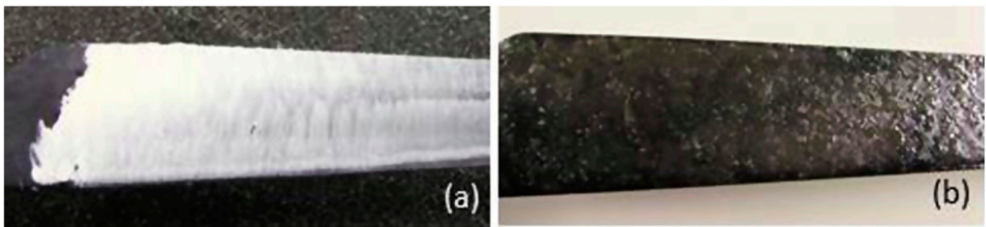


Fig. 4. (a) blade fouled with 1.1 mm thick layer of lithium grease impregnated with diatomaceous earth, (b) blade roughened with randomly applied contact cement. [42]

Marine biofouling is a process from being attached to biological reproduction which takes about three weeks [9]. By analyzing the images, the degree of attachment, consequently, the degree of fault could be estimated in time. This kind of diagnosis method has been applied in cancer image processing and achieved promised results, such as breast cancer diagnosis [31].

3. The Sparse Autoencoder and Softmax Regression based Diagnosis Method

The diagnosis method proposed in this paper is divided into four steps as shown in Figure 5. Step 1, preprocess the unlabeled images to pre-train the convolution kernels; Step 2, make the convolution between the labeled images and convolution kernels to obtain the convolved features of each image in the labeled samples; Step 3, transform the convolved features into the pooled features by using pooling operation; finally, Step 4, put the pooled features into the softmax classifier to diagnose the faults category .

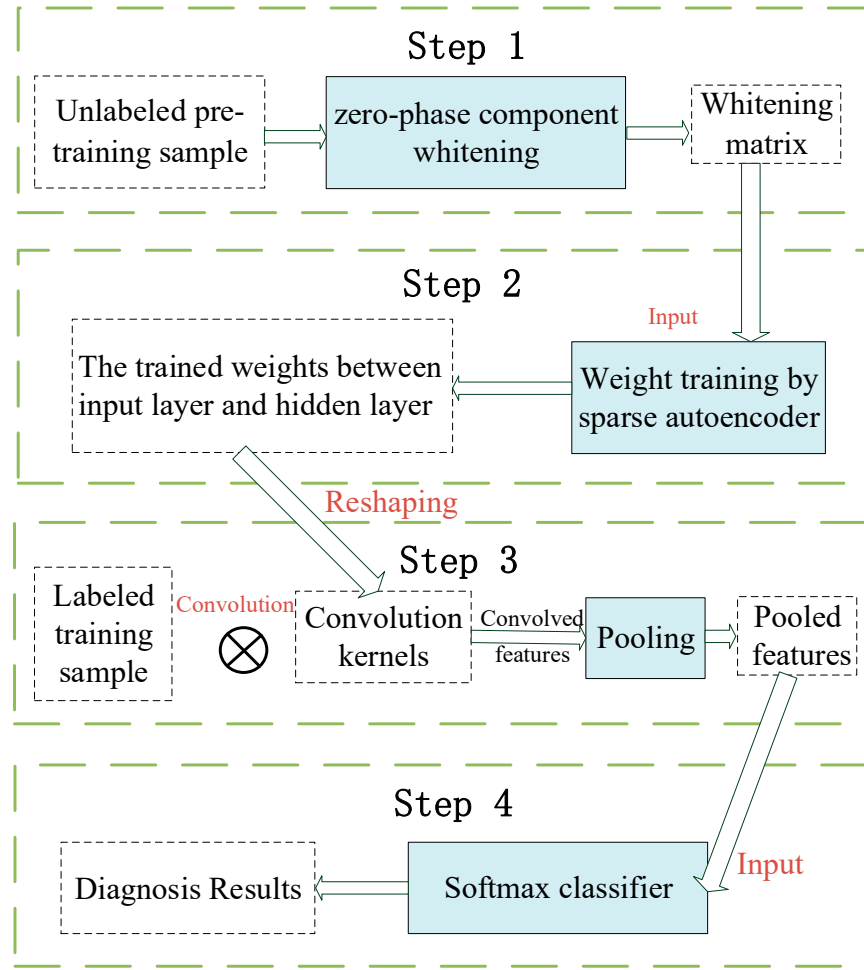


Figure 5. Frame of the proposed diagnosis method.

3.1. Image data preprocessing

The whole image of MCT will result in great number of parameters as input, and the 160 unlabeled images are used to extract patches for effectively extracting features. We extract 500 patches of 20×20 pixels per channel (3 channels for each patch) from each image as the unlabeled learning samples, which are arranged in matrix $\mathbf{X}_{unlabel} = [\mathbf{x}_{unlabel}^1, \dots, \mathbf{x}_{unlabel}^{80000}]$, where $\mathbf{x}_{unlabel}^k$ is the k th column of $\mathbf{X}_{unlabel}$, which is a matrix of dimension 1200×80000 , where $1200 = 20 \times 20 \times 3$ represents the amount of pixels of one patch and $80000 = 160 \times 500$ corresponds the total number of patches. Then we use the zero mean and zero-phase component (ZCA) whitening technique [32] to calculate matrix $\mathbf{X}_{whitening}$. The row images of MCT are effectively reduced by ZCA preprocessing so as to sparse autoencoder's input with low correlation.

$$\mathbf{x}_{unlabel}^{*k} = \mathbf{x}_{unlabel}^k - \frac{1}{m} \sum_{i=1}^m \mathbf{x}_{unlabel}^i \quad (1)$$

$$\mathbf{C}_X = \frac{1}{m} \mathbf{X}_{unlabel}^* (\mathbf{X}_{unlabel}^*)^T \quad (2)$$

$$\mathbf{X}_{whitening} = \mathbf{U}(\mathbf{S} + \varepsilon \mathbf{I})^{-\frac{1}{2}} \mathbf{X}_{unlabel}^* \quad (3)$$

Where $\mathbf{x}_{unlabel}^{*k}$ is the k th column of $\mathbf{X}_{unlabel}^*$; \mathbf{C}_X the covariance matrix of $\mathbf{X}_{unlabel}^*$; $m=80000$ the number of samples; \mathbf{S} is the diagonal matrix of eigenvalues and \mathbf{U} is the eigenvectors of \mathbf{C}_X , and ε is the regularization parameter.

3.2. Pre-training convolutional kernels based on sparse autoencoder

The recent image recognition of method is that the convolutional kernels and the softmax's parameters are trained based on convolution, and the number of convolutional layers is greater than one. The method of mentioned could extract abundant features by trained convolutional kernels for image with complex feature. however, network with less convolutional layers also shows good performance in some image classification. For instance, reference [36] uses two convolutional layers to classify different numbers, this paper tries to use one convolutional layer and asynchronously train convolutional kernels and softmax's parameters to classify MCT's image. Training convolutional kernels are based on SA.

Fig.6 shows the structure of SA neural network. It has three layers, the input layer (L_1), hidden layer (L_2) and output layer (L_3), where "+1" is the bias coefficient. SA is an unsupervised learning algorithm because its ideal output equals to its input, which means that it can learn features from training data by itself. Assuming the preprocessed input matrix $\mathbf{X}_{whitening} = [\mathbf{x}^1, \dots, \mathbf{x}^{80000}]$, where \mathbf{x}^k is the k th column of $\mathbf{X}_{whitening}$, $\mathbf{x}^k \in \mathbb{R}^n$, $n=1200$ is the number of pixels of each patch. $\mathbf{W}_{ji}^{(1)}$, for $i = 1, \dots, s_1, j = 1, \dots, s_2$, denotes the weight connecting the i th neuron from the input layer to the j th neuron of the hidden layer. The input threshold of the hidden layer is $\mathbf{b}^{(1)}$. $\mathbf{W}_{ij}^{(2)}$, for $i = 1, \dots, s_3, j = 1, \dots, s_2$, denotes the weight connecting the j th neuron from the hidden layer to the i th neuron of the output layer; where $s_1 = 1200$ is the number of neurons in the input layer, $s_2 = 800$ the number of neurons in the hidden layer, $s_3 = 1200$ the number of neurons in the output layer. The threshold of the output layer is $\mathbf{b}^{(2)}$. $\mathbf{W}_{ji}^{(1)}$, $\mathbf{W}_{ij}^{(2)}$, $\mathbf{b}^{(1)}$ and $\mathbf{b}^{(2)}$ are trainable parameters and which are trained by the forward and backward propagation method. The activation function of the hidden layer is the sigmoid function and that of the output layer is the proportional function. The optimal values of parameters are calculated by using L-BFGS algorithm [34]. Finally, the weights of the hidden layer are the learned features. After pretraining based on SA, the weights between input layer and hidden layer are reshaped for extracting the convolution features as convolutional kernels.

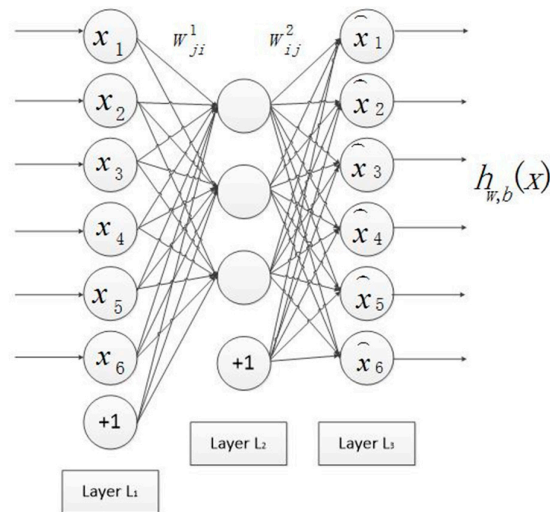


Figure 6. SA neural network structure.

$$\mathbf{z}_j^{(2)} = \sum_{i=1}^{s_1} \mathbf{W}_{ji}^{(1)} \mathbf{x}_i + \mathbf{b}_j^{(1)} \quad (4)$$

$$\mathbf{a}_j^{(2)} = f_1(\mathbf{z}_j^{(2)}) = \frac{1}{1 + \exp(-\mathbf{z}_j^{(2)})} \quad (5)$$

$$\mathbf{z}_i^{(3)} = \sum_{j=1}^{S_2} \mathbf{w}_{ij}^{(2)} \mathbf{a}_j^{(2)} + \mathbf{b}_i^{(2)} \quad (6)$$

$$\mathbf{a}_i^{(3)} = f_2(\mathbf{z}_i^{(3)}) = t \mathbf{z}_i^{(3)} \quad (7)$$

where \mathbf{x}_i is the i th component of vector \mathbf{x} , $\mathbf{z}_j^{(2)}$ and $\mathbf{a}_j^{(2)}$ correspond to the input and output of the activation function in the j th neurons of the hidden layer respectively, $\mathbf{z}_i^{(3)}$ and $\mathbf{a}_i^{(3)}$ correspond to the input and output of the activation function in the i th neuron of the output layer respectively, t is the proportionality coefficient. Assuming that the input is a dataset containing $m=80000$ samples.

3.3. Features Extraction based on Convolution and Pooling

Local connection and weight sharing are the characteristics of convolution layer, so using convolution can reduce the number of parameters and training complexity. In addition, the convolutional and pooling architecture can learn invariant features and reduce the over-fitting [35]. In this step, the convolved features will be extracted from each image firstly, then the pooled features will be obtained by sub-sampling the convolved features.

Different feature activation value is obtained at each location in the image by convolving each image with the convolution kernels pre-trained in the previous step. Specifically, if the number of pixels of one image is $D_{image} \times D_{image}$ and the number of pixels of convolution kernels is $D_{patch} \times D_{patch}$, the dimension of the convolved features is $(D_{image} - D_{patch} + 1) \times (D_{image} - D_{patch} + 1)$ [36]. Assuming the number of kernels for the hidden layer is equal to n_h , the dimension of a convolved feature is $(D_{image} - D_{patch} + 1) \times (D_{image} - D_{patch} + 1) \times n_h$ which will bring difficulty to classify.

Pooling operation is then introduced to reduce the dimension of the convolved features while maintaining the invariant information and to improve the results with less over-fitting. The mean pooling is used in this paper [36].

3.4. Faults classification based on softmax classifier

After step 3, the pooling features are obtained for training classifier. According to the different attachment degrees, the different categories and labels are set. The pooling features is as the softmax input. Suppose θ is a parameter matrix, the L-BFGS iterative algorithm can be used to obtain parameter θ .

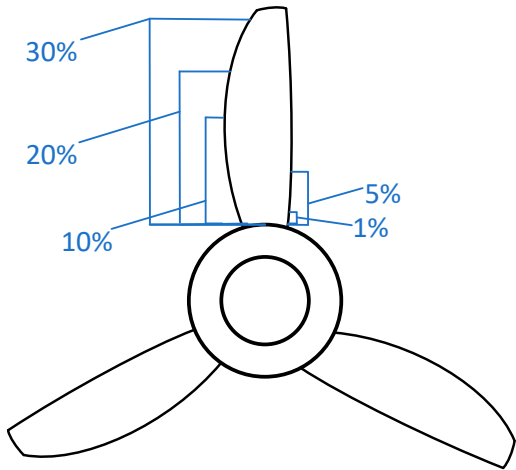
$$h_{\theta}(\mathbf{x}^{(i)}) = \begin{bmatrix} p(y^{(i)} = 1 | \mathbf{x}^{(i)}; \theta) \\ p(y^{(i)} = 2 | \mathbf{x}^{(i)}; \theta) \\ \vdots \\ p(y^{(i)} = k | \mathbf{x}^{(i)}; \theta) \end{bmatrix} = \frac{1}{\sum_{j=1}^k e^{\theta_j \mathbf{x}^{(i)}}} \begin{bmatrix} e^{\theta_1 \mathbf{x}^{(i)}} \\ e^{\theta_2 \mathbf{x}^{(i)}} \\ \vdots \\ e^{\theta_k \mathbf{x}^{(i)}} \end{bmatrix} \quad (8)$$

4. Experimental analysis

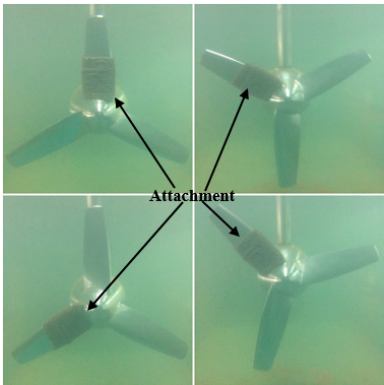
4.1. Experimental Platform

In order to get a rich diversity of samples, the state of each category will be sampled from the blade in 4 different configurations to extract data as shown in Figure 6. In this experiment, the speed of water current is set 0.6m/s. 860 images with RGB channels are collected by underwater camera, the camera is 1.2 million pixels. The sampling frequency is 1Hz. The luminous flux of fluorescent lamp is 1700lm. After remote transmission, each channel is represented by a matrix of size (320×320). Among them, 160 images are selected as

211 unlabeled pre-training samples, 420 images as labeled training samples, and the remaining
212 280 images as testing samples.
213 In this paper, for simplicity and without losing generality, we define eight categories according
214 to the proportion of the area covered by attachment, as shown in Figure 7.



215
216 **Figure 7.** Single blade with different degrees attachment.



217
218 **Figure 8.** Four configurations of blade data acquisition.

219
220 Figure 9 shows the experiment platform of MCT, it is a 230W direct-drive permanent magnet
221 synchronous motor prototype. The whole system mainly consists of three parts: 1) the permanent
222 magnet synchronous generator (PMSG) prototype; 2) the marine current simulation system
223 (adjustable flow rate from 0.2m/s to 1.5m/s); 3) the data monitoring and collection system. This
224 platform can simulate stationary current, wave and turbulence. Table III gives the main parameters
225 of the system.

226 **Table 1.** Diagnostic category label.

Percentage of area occupied by attachment (%)	(0,1]	(1,5]	(5,10]	(10,20]	(20,30]	60 (two blades, with each 30 attachment)	90 (three blades, with each 30 attachment)

Classifier labels	1	2	3	4	5	6	7
-------------------	---	---	---	---	---	---	---

Table 2. Detail of dataset.

Dataset's name	Number
Unlabeled pre-training sample	160
Labeled training sample	420
Testing sample	280

Table 3. Parameters of the MCT.

PMSG	SAP 71
Rated power	230W
Rated voltage	37V
Rated current	21A
Pole-pair number	8
Airfoil	Naca0018
Chord length	0.19m-0.32m
Blade diameter	0.6m

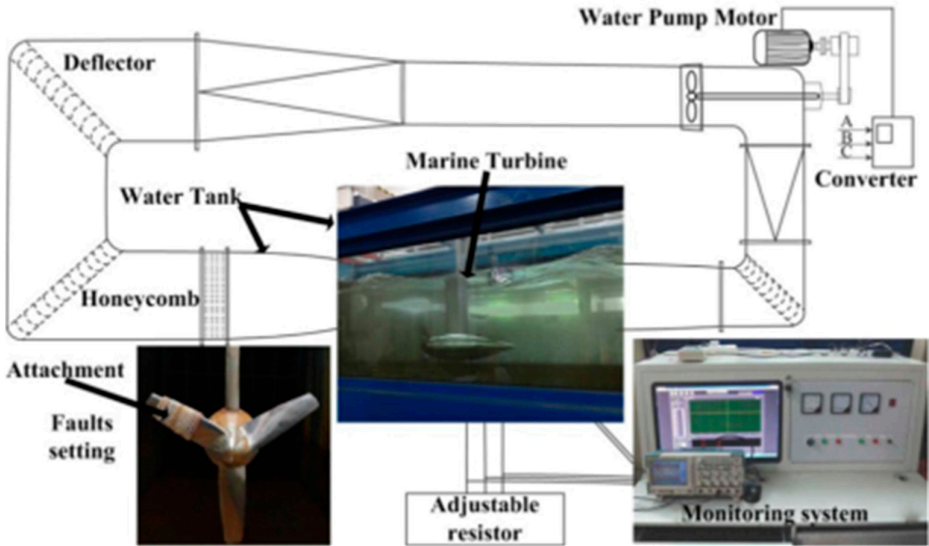


Figure 9. Experiment platform of the MCT [17].

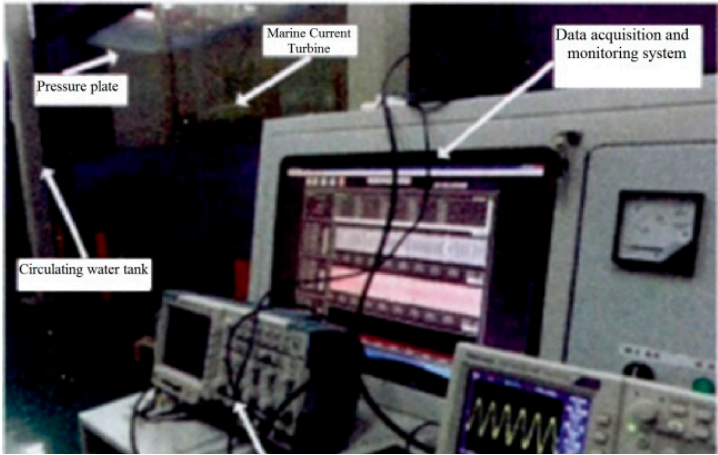


Figure 10. Data collection of the MCT.

4.2. Experimental Results and Comparison

Besides using the SA neural network for features extraction and softmax classifier for classification, this paper also uses CNN for features extraction and classification, PCA algorithm for features extraction and BP neural network for classification [38], and compares the results of different methods. The PCA algorithm is used to produce kernels from $X_{whitening}$ and the BP neural network is used to classify the faults, so combine the PCA algorithm with BP neural network can produce kernels and classify faults, which shows in Table V. Meanwhile compared CNN's weights is different for proposed method, because the kernels and softmax's parameters are simultaneously trained. Table IV gives all the parameters of SA in training step and Figure 11 gives its flow chart for all steps. The parameters of compared methods are shown in Table V.

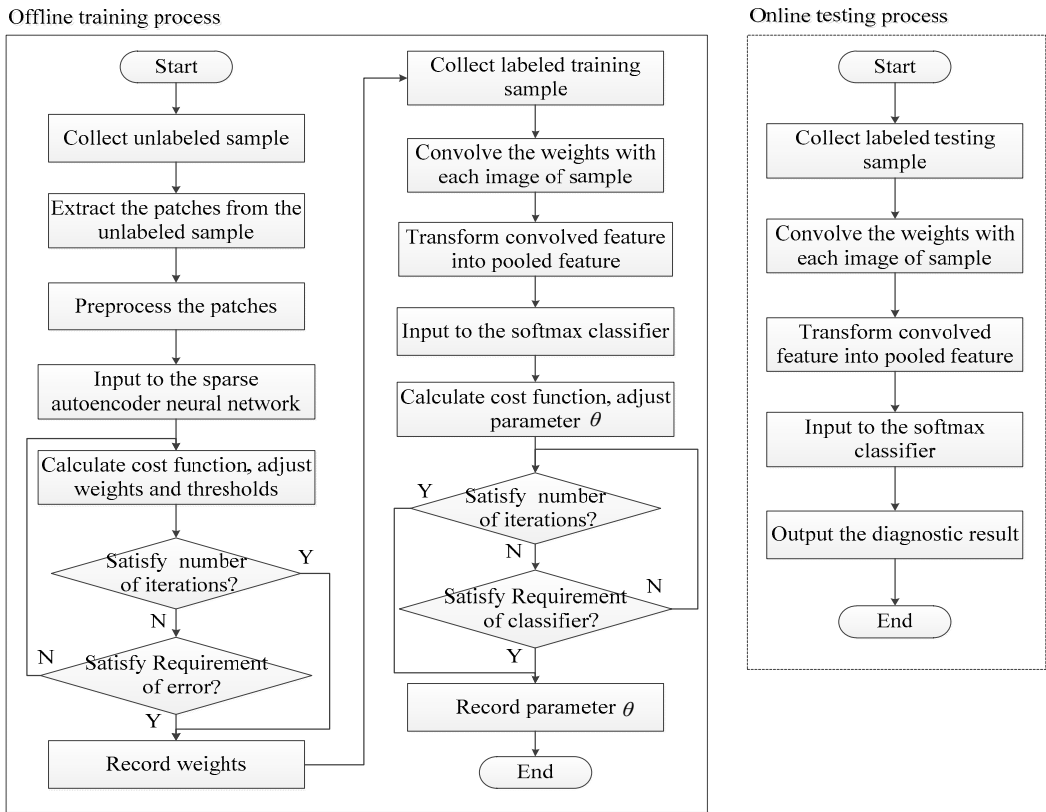


Figure 11. Training and testing flow chart.

246

Table 4. The parameters of the whole system.

Parameters	Significance	Value
ε	Whitening parameter	0.1
m	Number of training samples	80,000
λ_1	Weight attenuation parameter for SA	0.003
β	Weight of the sparsity penalty term	3
ρ	Sparsity parameter	0.1
λ_2	Weight attenuation parameter for softmax	0.0001
Hidden size	Number of neurons in the hidden layer	400
t	Proportionality coefficient	1

247

248

Table 5. The parameters of mentioned methods.

Mentioned methods	Parameters' name	Parameters
PCA	Cumulative percent variance	95% or 99%
BP (classifier)	Number of layers	2
	Loss function	Mean-square error
CNN	Number of convolutional layers	1
	Number of pooling layers	1
	Loss function	Cross entropy loss

249

Table 6. Experimental results based on different methods.

Diagnosis method		Accuracy		
		Test 1	Test 2	Average
PCA+ BP	CPV=95%	94.06%	87.81%	90.935%
	CPV=99%	80.94%	90.00%	85.47%
PCA+ softmax	CPV=95%	98.750%	98.750%	98.750%
	CPV=99%	98.750%	98.750%	98.750%
SA+BP		98.44%	96.25%	97.345%
SA+softmax		99.375%	99.375%	99.375%
CNN		98.75%	98.44%	98.60%

250

251

252

Experimental results show that with same method of features extraction, all the classifier method's results are very good. That means the representational characteristics are got by the proposed method. And the softmax classifier presents better performance than BP classifier. What's

more, the softmax classifier shows a stable diagnostic accuracy. The experimental results illustrate also that the feature extraction ability of SA is better than that of PCA whatever its value of CPV (95% or 99%).

5. Conclusions

Due to the hardness of MCT's working environment, underwater image is chosen as the fault diagnosing signal to classify the different degree of MCT's biological attachment. This paper proposes a diagnosis method based on a sparse autoencoder and softmax regression, which consists of four parts. 1) preprocessing the unlabeled images to pre-train the convolution kernels; 2) making the convolution between the labeled images and convolution kernels to obtain the convolved features of each image in the labeled samples; 3) transforming the convolved features into the pooled features by using pooling operation; 4) applying the pooled features into the softmax classifier to diagnose which category they belong to. The SA is used to product kernels and SR is used to classify them. Images are used to monitor whether the blade is attached by benthos and then to determine its corresponding degree of attachment. Also, this paper compares simultaneously training method (CNN) with other asynchronously training methods (PCA for kernel production and BP for classification). The experimental results and comparison with other methods show that the proposed method is useful to classify the different degree of biological attachment. However, the training time of the proposed method is too long, and we will simplify the algorithm and speed up the training speed in the future work.

Acknowledgement

This paper was supported by Shanghai Natural Science Foundation (16ZR1414300) and National Natural Science Foundation of China (61673260). Thank you very much for all reviewers. They gave this paper insightful advices and helps, which allow greatly improving this paper.

Conflicts of Interest: The authors declare no conflict of interest.

References

1. Muller, N.; Kouro, S.; Malinowski, M.; Rojas, C. A.; Jasinski, M.; Estay, G. Medium-voltage power converter interface for multi-generator marine energy conversion systems. *IEEE Transactions on Industrial Electronics*, **2016**, 64, 1061-1070.
2. Ferreira, R. M.; Estefen, S. F.; Romeiser, R. Under what conditions sar along-track interferometry is suitable for assessment of tidal energy resource. *IEEE Journal of Selected Topics in Applied Earth Observations & Remote Sensing*, **2017**, 9, 5011-5022.
3. Lawrence, J.; Sedgwick, J.; Jeffrey, H.; Bryden, I. An overview of the u.k. marine energy sector. *Proceedings of the IEEE*, **2013**, 101, 876-890.
4. Zhou, Z.; Benbouzid, M.; Charpentier, J. F.; Scuiller, F.; Tang, T. A review of energy storage technologies for marine current energy systems. *Renewable & Sustainable Energy Reviews*, **2013**, 18, 390-400.
5. Anwar, M. B.; Moursi, M. S. E.; Xiao, W. Dispatching and frequency control strategies for marine current turbines based on doubly fed induction generator. *IEEE Transactions on Sustainable Energy*, **2016**, 7, 262-270.
6. Goundar, J. N.; Ahmed, M. R. Marine current energy resource assessment and design of a marine current turbine for fiji. *Renewable Energy*, **2014**, 65, 14-22.
7. Chen, H.; At-Ahmed, N.; Machmoum, M.; Zam, E. H. Modeling and vector control of marine current energy conversion system based on doubly salient permanent magnet generator. *IEEE Transactions on Sustainable Energy*, **2015** 7, 409-418.
8. Chen, H.; Tang, T.; Ait-Ahmed, N.; Benbouzid, M. E. H.; Machmoum, M.; Zaim, E. H. Attraction, challenge and current status of marine current energy. *IEEE Access*, **2018**, 6, 12665-12685.
9. Cao, S.; Wang, J. D.; Chen, H. S.; Chen, D. R. Progress of marine biofouling and antifouling technologies. *Chinese Science Bulletin*, **2011**, 56, 598-612.

10. Hsu, H. H.; Selvaganapathy, P. R. Development of a low cost Hemin based dissolved oxygen sensor with anti-biofouling coating for water monitoring. *IEEE Sensors Journal*, **2014**, 14, 3400-4307.
11. Kavousi-Fard, A.; Su, W. A combined prognostic model based on machine learning for tidal current prediction. *IEEE Transactions on Geoscience & Remote Sensing*, **2017**, 55, 3108-3114.
12. Ren, Z.; Wang, K.; Li, W.; Jin, L.; Dai, Y. Probabilistic power flow analysis of power systems incorporating tidal current generation. *IEEE Transactions on Sustainable Energy*, **2017**, 8, 1195-1203.
13. Gao, Z.; Cecati, C.; Ding, S. X. A survey of fault diagnosis and fault-tolerant techniques—part i: fault diagnosis with model-based and signal-based approaches. *IEEE Transactions on Industrial Electronics*, **2015**, 62, 3757-3767.
14. Zhou, Z.; Scuiller, F.; Charpentier, J. F.; Benbouzid, M. E. H.; Tang, T. Power smoothing control in a grid-connected marine current turbine system for compensating swell effect. *IEEE Transactions on Sustainable Energy*, **2013**, 4, 816-826.
15. Zhang, M.; Wang, T.; Tang, T.; Benbouzid, M.; Diallo, D. Imbalance fault detection of marine current turbine under condition of wave and turbulence. *IECON 2016 - 42nd Annual Conference of the IEEE Industrial Electronics Society*; Florence, 2016; pp. 6353-6358.
16. Zhang, M.; Wang, T.; Tang, T. A multi-mode process monitoring method based on mode-correlation PCA for Marine Current Turbine. *2017 IEEE 11th International Symposium on Diagnostics for Electrical Machines; Power Electronics and Drives (SDEMPED)*, Tinos, 2017; pp. 286-291.
17. Zhang, M.; Tang, T.; Wang, T. (2017). Multi-domain reference method for fault detection of marine current turbine. *IECON 2017 - 43rd Annual Conference of the IEEE Industrial Electronics Society*, Beijing, 2017, pp. 8087-8092.
18. Alvarez, A.; Caiti, A.; Onken, R. Evolutionary path planning for autonomous underwater vehicles in a variable ocean. *IEEE Journal of Oceanic Engineering*, **2004**, 29, 418-429.
19. McGee, J.; Catipovic, J.; Schoenecker, S.; Swaszek, P. Interference suppression in congested undersea environments. *OCEANS 2015 - Genova, Genoa*, 2015; pp. 1-8.
20. Krishna, C. R.; Yadav, P. S. A hybrid localization scheme for Underwater Wireless Sensor Networks. *International Conference on Issues and Challenges in Intelligent Computing Techniques*, **2017**, 4, 579-582.
21. Huang, L.; Zhao, X.; Huang, X.; Liu, Y. Underwater camera model and its use in calibration. *2015 IEEE International Conference on Information and Automation*, Lijiang, 2015; pp. 1519-1523.
22. Cho, H.; Jeon, H.; Yu, S. C.; Lee, J. K.; Jeon, M. Development of all-in-one-type deep-sea camera for monitoring Red Snow-crab habitats. *OCEANS 2016 MTS/IEEE Monterey*, Monterey, CA, 2016; pp. 1-5.
23. Xie, J.; Zhou, J. Classification of urban building type from high spatial resolution remote sensing imagery using extended mrs and soft bp network. *IEEE Journal of Selected Topics in Applied Earth Observations & Remote Sensing*, **2017**, 10, 3515-3528.
24. Wang, Z.; Shao, Y. H.; Bai, L.; Deng, N. Y. Twin support vector machine for clustering. *IEEE Trans Neural Netw Learn Syst*, **2015**, 26, 2583-2588.
25. R jichi, S.; Chaabane, F. Feature extraction using PCA for VHR satellite image time series spatio-temporal classification. *2015 IEEE International Geoscience and Remote Sensing Symposium (IGARSS)*, Milan, 2015; pp. 485-488.
26. He, K.; Zhang, X.; Ren, S.; Sun, J. (2015). Deep residual learning for image recognition. *2016 IEEE Conference on Computer Vision and Pattern Recognition (CVPR)*, Las Vegas, NV, 2016; pp. 770-778.
27. Szegedy, C.; Liu, W.; Jia, Y.; Sermanet, P.; Reed, S.; Anguelov, D. Going deeper with convolutions. *2015 IEEE Conference on Computer Vision and Pattern Recognition (CVPR)*, Boston, MA, 2015; pp. 1-9.
28. Freeman, I.; Roesse-Koerner, L.; Kummert, A. (2018). Effnet: an efficient structure for convolutional neural networks. *2018 25th IEEE International Conference on Image Processing (ICIP)*, Athens, Greece, 2018; pp. 6-10.
29. Wen, P.; Wang, T.; Xin, B.; Tang, T.; Wang, Y. Blade imbalanced fault diagnosis for marine current turbine based on sparse autoencoder and softmax regression. *2018 33rd Youth Academic Annual Conference of Chinese Association of Automation (YAC)*, Nanjing, 2018; pp. 246-251.
30. Hou, G.; Pan, Z.; Huang, B.; Wang, G.; Luan, X. Hue preserving-based approach for underwater colour image enhancement. *Iet Image Processing*, **2018**, 12, 292-298.
31. Endre, S.; Michal Z.; Eyras, E. Detection of recurrent alternative splicing switches in tumor samples reveals novel signatures of cancer. *Nucleic Acids Research*, **2015**, 43, 1345-56.

353 32. Krsman, V. D.; Sarić, A. T. Bad area detection and whitening transformation-based identification in three-
354 phase distribution state estimation. *Iet Generation Transmission & Distribution*, **2017**, 11, 2351-2361.
355 33. Tao, C.; Pan, H.; Li, Y.; Zou, Z. Unsupervised spectral-spatial feature learning with stacked sparse
356 autoencoder for hyperspectral imagery classification. *IEEE Geoscience & Remote Sensing Letters*, **2015**, 12,
357 2438-2442.
358 34. Ge, F.; Ju, Y.; Qi, Z.; Lin, Y. Parameter estimation of a gaussian mixture model for wind power forecast
359 error by Riemann l-bfgs optimization. *IEEE Access*, **2018**, 99, 1-1.
360 35. Norouzi, M.; Ranjbar, M.; Mori, G. Stacks of convolutional Restricted Boltzmann Machines for shift-
361 invariant feature learning. 2009 IEEE Conference on Computer Vision and Pattern Recognition, Miami, FL,
362 2009; pp. 2735-2742.
363 36. LÉcun, Y; Bottou, L, Bengio, Y; Haffner, P. Gradient-based learning applied to document recognition.
364 *Proceedings of the IEEE*, **1998**, 86, 2278-2324.
365 37. Wang, G.; Sim, K. C. Regression-based context-dependent modeling of deep neural networks for speech
366 recognition. *IEEE/ACM Transactions on Audio Speech & Language Processing*, **2014**, 22, 1660-1669.
367 38. Rad, S. J. M.; Tab, F. A.; Mollazade, K. Classification of Rice Varieties Using Optimal Color and Texture
368 Features and BP Neural Networks. 2011 7th Iranian Conference on Machine Vision and Image Processing,
369 Tehran, 2011; pp. 1-5.
370 39. Zubko, V.; Kaufman, Y. J.; Burg, R. I.; Martins, J. V. Principal component analysis of remote sensing of
371 aerosols over oceans. *IEEE Transactions on Geoscience & Remote Sensing*, **2007**, 45, 730-745.
372 40. Zhiqiang G. Process data analytics via probabilistic latent variable models: A tutorial review. *Industrial &*
373 *Engineering Chemistry Research*, 2018, 57, 12646-12661.
374 41. Tianzhen W.; Lei L.; Jiahui Z.; Emmanuel S.; Yide W. A M-EKF fault detection strategy of insulation system
375 for marine current turbine. *Mechanical Systems and Signal Processing*, 2019, 15, 269–280
376 42. Walker, J. M.; Flack, K. A.; Lust, E. E.; Schultz, M. P.; Luznik, L. Experimental and numerical studies of
377 blade roughness and fouling on marine current turbine performance. *Renewable Energy*, 2014, 66(66), 257-
378 267.